

# An implicit method for radiative transfer with the diffusion approximation in SPH

Serge Viau, Pierre Bastien

*Département de Physique and Observatoire du Mont-Mégantic, Université de Montréal,  
C.P. 6128, Succ. centre-ville, Montréal, Quebec, Canada*

serge.viau@collanaud.qc.ca; bastien@astro.umontreal.ca

and

Seung-Hoon Cha

*Département de Physique and Observatoire du Mont-Mégantic, Université de Montréal,  
C.P. 6128, Succ. centre-ville, Montréal, Quebec, Canada,*

*and*

*Korea Astronomy and Space Science Institute, 61-1, Whaam-Dong, Youseong-Gu, Taejeon,  
Korea*

cha@kasi.re.kr

## ABSTRACT

An implicit method for radiative transfer in SPH is described. The diffusion approximation is used, and the hydrodynamic calculations are performed by a fully three-dimensional SPH code. Instead of the energy equation of state for an ideal gas, various energy states and the dissociation of hydrogen molecules are considered in the energy calculation for a more realistic temperature and pressure determination. In order to test the implicit code, we have performed non-isothermal collapse simulations of a centrally condensed cloud, and have compared our results with those of finite difference calculations performed by MB93. The results produced by the two completely different numerical methods agree well with each other.

*Subject headings:* hydrodynamics – method: numerical – radiative transfer

## 1. Introduction

In order to understand the various stages of star formation it is essential to follow the exact thermal evolution of a collapsing cloud because some important dynamical processes, for example fragmentation (Silk 1977; Low & Lynden-Bell 1976; Rees 1976; Smith 1977; Bell & Lin 1994; Lodato & Clarke 2004), are closely related to the thermal evolution. The thermal evolution of a collapsing cloud is described by radiation hydrodynamics, and inevitably involves a numerical solution. However, it is not easy to implement and run a multi-dimensional radiation hydrodynamic code, so various approximate methods have been used instead of solving the full radiation hydrodynamic equations directly.

Yorke (1979, 1980); Masunaga et al. (1998); Masunaga & Inutsuka (2000) used one-dimensional hydrodynamic codes including a more realistic approach to radiative transfer. Such an approach can track the exact thermal evolution of a collapsing cloud, and is easily compared to the observational results. However, in a one-dimensional code it is impossible to observe some important dynamics, for example fragmentation.

On the other hand, a simplified treatment for the radiative transfer is needed in multi-dimensional hydrodynamic codes. The Eddington approximation was used by Winkler & Newman (1980a,b); Boss (1984); Myhill & Boss (1993), while Larson (1969) used the diffusion approximation in his one-dimensional simulations.

However, the multi-dimensional calculations with radiative transfer published so far have been done mostly with codes using the finite difference method. Although smooth particle hydrodynamics (hereafter SPH) codes are now used quite commonly in the calculations for self-gravitating clouds, so far few attempts<sup>1</sup> to include radiative transfer in an SPH code have been published (Lucy 1977; Brookshaw 1985; Whitehouse & Bate 2004). The main reason is that the diffusion approximation for treating radiative transfer there has a double differential in spatial coordinates which is very difficult to evaluate accurately with SPH because the particles occupy in principle arbitrary positions. Brookshaw (1985, hereafter B85) derived an equation which bypasses the double differential by converting it to a single differential. Cleary & Monaghan (1999, hereafter CM99) extended the B85 method to treat

---

<sup>1</sup>Whitehouse & Bate (2004) was published after the original work of Viau (2001), so we need to emphasize the differences between their approach and ours. First of all, Whitehouse & Bate (2004) concentrated on one-dimensional tests while this paper presents a fully three-dimensional calculation. Our test calculations are shown in Section 3. Furthermore, a more realistic energy calculation has been used in our code rather than the ideal equation of state. Details about the energy calculation are presented in Section 2. On the other hand, Whitehouse & Bate (2004) used a more detailed treatment of the radiative transfer which allows the radiation and gas temperature to be different.

cases with a discontinuous conductivity.

Another difficulty in the treatment of radiative transfer is the large difference in time scales. The radiative time scale is much shorter than the dynamical time scale in a collapsing cloud. Therefore, an implicit numerical scheme is needed to treat the thermal and dynamical evolutions simultaneously. Viau (2001) developed an effective implicit scheme for radiative transfer in a fully three-dimensional SPH code after many unsuccessful attempts.

We have performed a non-isothermal cloud collapse with the implicit code, and compared our results with those of Myhill & Boss (1993, hereafter MB93). The comparison should be useful because the two methods are completely different from each other.

The implicit scheme which combines the diffusion approximation and SPH is described in section 2 in detail. We have used a more realistic energy calculation instead of an ideal equation of state for the determination of temperature, and the detailed procedure for the specific internal energy calculation is also given in the same section. The non-isothermal cloud collapse simulations and the comparison of our results with those of MB93 are given in section 3. The summary is in section 4.

## 2. Numerical methods

### 2.1. Smoothed Particle Hydrodynamics : SPH

SPH (Lucy 1977; Gingold & Monaghan 1977) is a grid-free and fully Lagrangian method, and therefore has been widely used in gravitational collapse simulations. The Lagrangian hydrodynamics with self-gravitation are given by

$$\frac{D\rho}{Dt} = -\rho\nabla \cdot \mathbf{v}, \quad (1)$$

$$\frac{D\mathbf{v}}{Dt} = -\frac{1}{\rho}\nabla P - \nabla^2\Phi, \quad (2)$$

$$\frac{Du}{Dt} = -\frac{P}{\rho}\nabla \cdot \mathbf{v}, \quad (3)$$

where  $D/Dt$  is the Lagrangian derivative,  $u$  is the specific internal energy and other variables have their usual meaning. Although there are many alternatives for the SPH formulation of equations (1) – (3) (Monaghan 1992; Hernquist & Katz 1989), we have used a common form given by

$$\rho = \sum_j m_j W_{ij}, \quad (4)$$

$$\frac{\Delta \mathbf{v}}{\Delta t} = - \sum_j m_j \left( \frac{P_i}{\rho_i^2} + \frac{P_j}{\rho_j^2} + \Pi_{ij} \right) \nabla_i W_{ij} - \nabla^2 \Phi_i, \quad (5)$$

$$\frac{\Delta u}{\Delta t} = \frac{1}{2} \sum_j m_j \left( \frac{P_i}{\rho_i^2} + \frac{P_j}{\rho_j^2} + \Pi_{ij} \right) (\mathbf{v}_i - \mathbf{v}_j) \cdot \nabla_i W_{ij}. \quad (6)$$

Here  $\Pi_{ij}$  is the artificial viscosity given by

$$\frac{-\alpha \bar{c}_{s,ij} \mu_{ij} + \beta \mu_{ij}^2}{\bar{\rho}_{ij}}, \quad (7)$$

where  $\mu_{ij} = h \frac{\mathbf{v}_{ij} \cdot \mathbf{r}_{ij}}{r_{ij}^2 + \eta^2}$ ,  $h$  is the smoothing length,  $\mathbf{v}_{ij} = \mathbf{v}_i - \mathbf{v}_j$ ,  $\mathbf{r}_{ij} = \mathbf{r}_i - \mathbf{r}_j$ ,  $\bar{c}_{s,ij} = (c_{s,i} + c_{s,j})/2$ ,  $\bar{\rho}_{ij} = (\rho_i + \rho_j)/2$ , and  $\alpha$ ,  $\beta$  and  $\eta$  are free parameters<sup>2</sup>. Here  $c_s$  is the sound speed. Although the artificial viscosity has a side-effect in differentially rotating systems (Monaghan 1989; Morris & Monaghan 1997; Cha & Whitworth 2003b), it is essential for the treatment of shock waves in SPH.  $W$  in equations (4) - (6) is a kernel function, and the M4 kernel (Monaghan & Lattanzio 1984) has been used in our simulations. For additional details about SPH, the reader is referred to the reviews by Benz (1990) and Monaghan (1992).

## 2.2. Diffusion approximation in SPH

The diffusion approximation has been adopted in our three-dimensional SPH code for the treatment of radiative transfer, because it is very hard to trace the exact behavior of individual photons in the multi-dimensional hydrodynamic code (but see Oxley & Woolfson 2003). The diffusion approximation is strictly valid only for regions of great optical depth (i.e. optically thick medium). However, the early stage of the collapse of a cloud is optically thin because of the very low density and effective cooling. Larson (1969) discussed this point in his one-dimensional simulations, and concluded that the diffusion approximation can be applied in the isothermal stage of a collapsing cloud, because the diffusion approximation essentially keeps the cloud temperature at the boundary value in the early stage of the collapse.

The energy equation with the diffusion term is given by

$$\frac{Du}{Dt} = -\frac{P}{\rho} \nabla \cdot \mathbf{v} - \frac{1}{\rho} \nabla \cdot \mathbf{F}, \quad (8)$$

---

<sup>2</sup>We have used  $\alpha = 1.0$ ,  $\beta = 2.0$  and  $\eta = 0.1$  in all simulations.  $\eta$  is not a critical free parameter (Monaghan 1997) for the artificial viscosity, because normally  $\mathbf{r}_i \neq \mathbf{r}_j$ .

where  $\mathbf{F}$  is the radiative flux, and is given by

$$\mathbf{F} = -\frac{4acT^3}{3\kappa_R\rho}\nabla T, \quad (9)$$

where  $\kappa_R$  is the Rosseland mean opacity,  $a$  is  $\frac{4\sigma_{SB}}{c}$ ,  $c$  is the speed of light and  $\sigma_{SB}$  is the Stephan–Boltzmann constant. If an effective conductivity,  $Q(\equiv -\frac{16\sigma_{SB}T^3}{3\kappa_R\rho})$  is defined, equation (8) may be rewritten as

$$\frac{Du}{Dt} = -\frac{P}{\rho}\nabla \cdot \mathbf{v} - \frac{1}{\rho}\nabla \cdot (Q\nabla T). \quad (10)$$

Equation (10) contains a double derivative, and this  $\nabla^2$  operation is very sensitive to the disorder in the particle distribution, such that it may cause numerical noise in the simulation. B85 suggested another formulation for the diffusion term to avoid this  $\nabla^2$  operator. We describe here briefly the treatment of B85.

In one–dimension, the diffusion term of equation (10) becomes

$$\frac{1}{\rho} \left( \frac{dQ}{dx} \frac{dT}{dx} + Q \frac{d^2T}{dx^2} \right). \quad (11)$$

The derivation for the first term of equation (11) starts from the Taylor expansions of  $T(x')$  and  $Q(x')$  around  $T(x)$  and  $Q(x)$ , respectively,

$$Q(x') = Q(x) + (x' - x) \frac{dQ}{dx} + \frac{1}{2}(x' - x)^2 \frac{d^2Q}{dx^2} + \dots, \quad (12)$$

$$T(x') = T(x) + (x' - x) \frac{dT}{dx} + \frac{1}{2}(x' - x)^2 \frac{d^2T}{dx^2} + \dots. \quad (13)$$

From equations (12) and (13) one can derive,

$$[Q(x') - Q(x)][T(x') - T(x)] = (x' - x)^2 \frac{dQ}{dx} \frac{dT}{dx}, \quad (14)$$

and the integral interpolant form of equation (14) becomes

$$\frac{dQ}{dx} \frac{dT}{dx} = - \int \frac{[Q(x') - Q(x)][T(x') - T(x)]}{x - x'} \frac{\partial W(x - x')}{\partial x} dx'. \quad (15)$$

For the derivation of the second term of equation (11), we will use equation (13),

$$- \int \frac{T(x') - T(x)}{x - x'} \frac{\partial W(x - x')}{\partial x} dx' = \int \frac{dT}{dx} \frac{\partial W(x - x')}{\partial x} dx' - \frac{1}{2} \int (x - x') \frac{d^2T}{dx^2} \frac{\partial W(x - x')}{\partial x} dx', \quad (16)$$

and it becomes

$$Q \frac{d^2 T}{dx^2} = -2Q \int \frac{T(x') - T(x)}{x - x'} \frac{\partial W(x - x')}{\partial x} dx'. \quad (17)$$

From equations (15) and (17), the diffusion term of equation (8) in one-dimension becomes

$$\frac{1}{\rho} \left( \frac{dQ}{dx} \frac{dT}{dx} + Q \frac{d^2 T}{dx^2} \right) = \sum_j \frac{m_j}{\rho_i \rho_j} \frac{(Q_i + Q_j)(T_i - T_j)}{x_i - x_j} \frac{\partial W_{ij}}{\partial x_i}, \quad (18)$$

and the three-dimensional form becomes

$$\frac{1}{\rho} (\nabla Q \cdot \nabla T + Q \nabla^2 T) = \sum_j \frac{m_j}{\rho_i \rho_j} \frac{(Q_i + Q_j)(T_i - T_j)}{|\mathbf{r}_i - \mathbf{r}_j|^2} (\mathbf{r}_i - \mathbf{r}_j) \cdot \nabla_i W_{ij}. \quad (19)$$

With equation (18) or (19), the calculation of  $\nabla^2$  can be avoided, and the energy equation becomes finally

$$\frac{\Delta u}{\Delta t} = \frac{1}{2} \sum_j m_j \left( \frac{P_i}{\rho_i^2} + \frac{P_j}{\rho_j^2} + \Pi_{ij} \right) (\mathbf{v}_i - \mathbf{v}_j) \cdot \nabla_i W_{ij} + \sum_j \frac{m_j}{\rho_i \rho_j} \frac{(Q_i + Q_j)(T_i - T_j)}{|\mathbf{r}_i - \mathbf{r}_j|^2} (\mathbf{r}_i - \mathbf{r}_j) \cdot \nabla_i W_{ij}. \quad (20)$$

This method derived by B85 is valid for a constant or smoothly varying conductivity. CM99 suggested a modification to treat media with a discontinuous conductivity. They considered the continuity of conductive heat flux across the border of adjacent cells (or particles), and found a better expression,  $\frac{4Q_i Q_j}{Q_i + Q_j}$ , for the effective conductivity term instead of  $(Q_i + Q_j)$  in equation (20). CM99 also performed various tests with the new formulation, and some of them are repeated in the next section.

### 2.3. Test of the new formulation: thermal conduction

Given the approximation involved in the derivation presented above, it is not obvious that a solution of equation (20) is also a solution of equation (8). Therefore we have performed a test of the thermal conduction problem to verify the treatment for the double derivative. The thermal diffusion equation is given by

$$\rho \frac{du}{dt} = \nabla \cdot (\kappa \nabla T), \quad (21)$$

where  $t$  is time and  $\kappa$  is the thermal conductivity. The simplest case for the thermal diffusion equation is that  $\kappa$  is a constant (i.e. a homogeneous medium). In this case equation (21) becomes

$$\frac{dT}{dt} = \frac{\kappa}{\rho \sigma} \nabla^2 T. \quad (22)$$

Here a simple relation between  $u$  and  $T$ ,  $u = \sigma T$  is assumed, and  $\sigma$  is the specific heat of the medium. The treatments of B85 and CM99 are the same in this simple case, and so equation (22) can be rewritten as

$$\frac{\Delta T}{\Delta t} = \frac{2\kappa}{\rho_i \sigma} \sum_j \frac{m_j}{\rho_j} \frac{T_i - T_j}{x_i - x_j} \frac{\partial W_{ij}}{\partial x_i} \quad (23)$$

in one–dimension.

For this test, we have used 40 particles in  $0 \leq x \leq \pi$ , and a constant  $h$  value for all particles.  $\rho$ ,  $\sigma$  and  $\kappa$  are set to unity, and all particles keep their original positions in this test, so the situation is very similar to a one–dimensional finite difference simulation. The temperature distribution at  $t = 0$  is given by

$$T(x, 0) = \sin x, \quad (24)$$

and the boundary temperature is set to 0K. The analytic solution of equation (22) is,

$$T(x, t) = e^{-t} \sin x. \quad (25)$$

Figure 1 shows the results until  $t = 2$ . The solid lines in the figure are the analytic solution given by equation (25) at different times, and the dots are the results of our numerical calculation. The numerical solution reproduces the analytic solution very well and confirms the validity of the B85 formulation. Furthermore we have performed several tests for cases with a discontinuous conductivity as presented in CM99. We will show one of them. In this test the medium is divided into two parts, and each part has different values for the conductivity, so the resultant diffusivity ( $\equiv \frac{\kappa}{\rho\sigma}$ ) is different in the left and right part of the medium. The initial conditions for this test are shown in Table 1. Refer to section 5.3 of CM99 for details of this test. Figure 2 shows the results. The method of B85 as modified by CM99 (open circles) is more accurate than the original one by B85 (crosses). We have used the the modification suggested by CM99 in our three–dimensional test (See section 3).

Table 1: Initial conditions for discontinuous conductivity test

	left	right
$T$	0	1
$\rho$	1	1
$\kappa$	10	1
$\sigma$	1	1

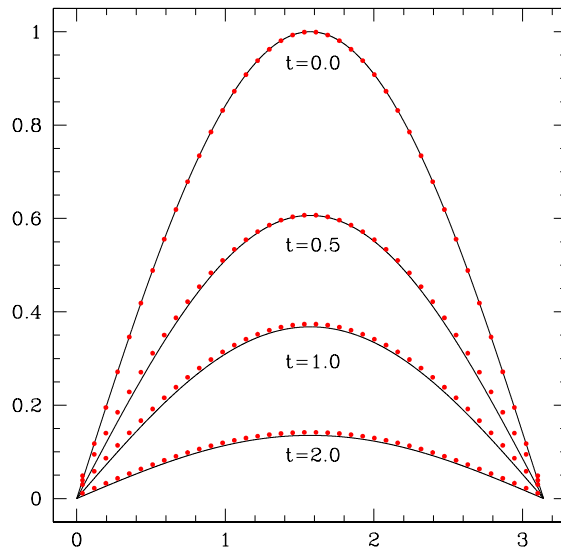


Fig. 1.— A numerical solution for the heat conduction equation at  $t = 0.0, 1.0, 1.5$  and  $2.0$ . The dots are the numerical solution using equation (23), and the solid lines are the analytic solution given by equation (25). There is very good agreement between these two solutions. The boundary temperature is set to 0K in this simulation.



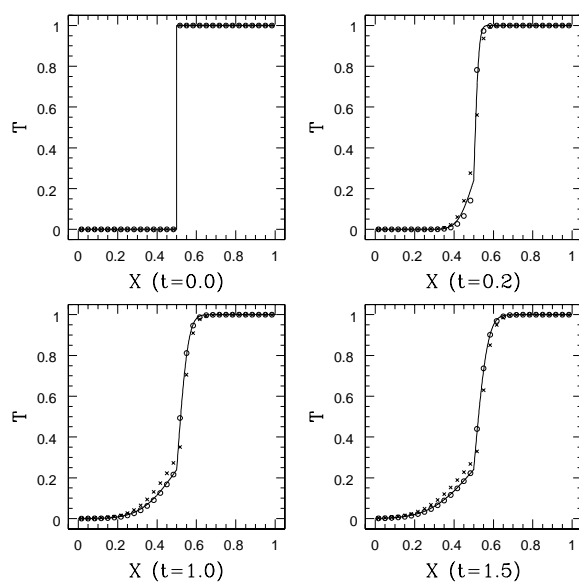


Fig. 2.— Numerical solutions for the heat conduction equation with different conductivity at  $t = 0.0, 0.2, 1.0$  and  $1.5$ . The open circles are with the expression of CM99, and the crosses are with the original method of B85, respectively. The analytic solution is drawn by a solid line. From  $t = 0.2$ , the numerical results show small deviations from the analytic solution. Generally speaking, the modification of CM99 shows a better agreement than B85.

## 2.4. Implicit scheme for radiative transfer

The radiative time scale is much shorter than the dynamical time scale in a collapsing cloud, so the numerical integration of equation (20) is not easy. An implicit scheme has been developed to treat the radiative transfer and the dynamical evolution simultaneously (Viau 2001), and we explain each step of this implicit scheme.

1. Define a function  $\mathcal{F}$  from equation (8),

$$\mathcal{F} = u_i^* - u_i^0 + \delta t \left( \frac{P}{\rho} \nabla \cdot \mathbf{v} \right)_i^0 + \delta t \left( \frac{1}{\rho} \nabla \cdot \mathbf{F} \right)_i^*, \quad (26)$$

where  $u_i^0$  is the former step value, and  $u_i^*$  is the new value updated by the iteration. The second and third terms of equation (26) are known for each time step. The goal of the iteration is to find the value of  $u_i^*$  (or equivalently  $T_i^*$ ) which will bring  $\mathcal{F} = 0$ .

2. Set the boundary values for temperature,  $T_L$  and  $T_R$ . These boundary temperatures are initially limited by the temperature range of the opacity table (see section 2.5).
3. Find  $u_L$  and  $u_R$  from  $T_L$  and  $T_R$ , respectively. At this stage various energy states and the dissociation of hydrogen molecules are considered (see section 2.6).
4. Find the median value,  $T_i^*$  using the bisection method or the Van Wijngaarden–Dekker–Brent method (e.g. Press et al. 1992). The convergence speed of the Van Wijngaarden–Dekker–Brent method is higher than that of the bisection method. Typically  $\sim 10$  iterations are required to solve equation (26) for one particle. This iteration is started using  $u_i^* = u_i^0$  as the initial guess. Rapid convergence here is a concern since we are in a double loop in the code.
5. Find  $u_i^*$  from  $T_i^*$
6. After all values of  $u_i^*$  have been found, we compute  $\mathcal{F}$  again using equation (26) with the new  $u_i^*$ . Note that only the first and fourth terms change in equation (26).
7. Repeat steps 4–6 until  $\mathcal{F} < tol$  for all particles, using the latest  $u_i^*$  found for each particle.

The tolerance,  $tol$  in step 6 is closely related to the resolution (and speed as well) of the calculation, and set to  $10^{-5}$  in our simulations. Typically several iterations ( $\leq 10$ ) are required to reach the desired precision.

In the procedure explained above, note that only the temperature and specific internal energy are updated at every iteration, while the pressure and density are fixed. The Rosseland mean opacity,  $\kappa_R$  is also updated by the corresponding temperature and fixed density. This whole procedure is executed for each particle separately, i.e. the new temperature is determined for each particle while keeping all the other particles at their original temperature. The convergence according to the same criterion has to be satisfied for all particles. If not, the above procedure is repeated until it is satisfied.

For comparison, the classical method to solve for the gravitational force for the  $N$ -body problem involves  $N^2/2$  steps. Using a tree approach brings this to  $N \log N$ . Here the radiative flux equation has to be solved simultaneously for all particles. When the specific energy for one particle is varied, all the other ones are fixed. In summary, this method is in  $N^2$  steps, times the number of iterations required. This is the price to pay for the different time scales between the radiative and dynamical events. But the method converges well and yields very good results. The number of iterations required allows taking larger time steps.

As an example, we have used a small Altix (Intel Itanium2 processor) for the calculations with 50000 particles reported below. The results were obtained with our serial code version, and the calculation time is just about an hour. We stopped the calculation when the maximum density (this happens usually at the cloud center) reaches  $10^5$  times the initial density. Generally speaking, the RHD calculation takes  $\approx 10$  times more CPU time than the HD calculation without radiative transfer.

The detailed procedures to derive  $\kappa_R$  and the specific internal energy from a given temperature will be described in sections 2.5 and 2.6, respectively.

## 2.5. Rosseland mean opacity

The Rosseland mean opacity,  $\kappa_R$  should be determined in order to implement radiative transfer in the diffusion approximation. The definition of the Rosseland mean opacity is given by

$$\frac{1}{\kappa_R} = \frac{\int_0^\infty \frac{1}{\kappa_\nu} \frac{dB_\nu}{dT} d\nu}{\frac{dB}{dT}}, \quad (27)$$

where  $B_\nu$  is the blackbody function at a frequency  $\nu$  and  $B$  is the frequency integrated blackbody function ( $\equiv \int_0^\infty B_\nu d\nu$ ).  $\kappa_\nu$  in equation (27) is determined by

$$\kappa_\nu = \frac{1}{\rho} n Q_{ext} \pi r_d^2, \quad (28)$$

where  $n$  is the number density,  $Q_{ext}$  and  $r_d$  are the extinction factor and size of dust grains. In the lower temperature range ( $T < 316\text{K}$ ), we have used the model for  $\kappa_\nu$  developed by Yorke (1979) with the more recent values for the extinction factor,  $Q_{ext}$  provided by Preibisch et al. (1993). The Rosseland mean opacity for this lower temperature region is shown in Figure 3. In the figure, the opacity jumps at  $T \simeq 125\text{K}$  because of the sublimation of the ice mantle on dust grains. In the higher temperature region ( $708\text{K} < T < 12500\text{K}$ ), we have used the

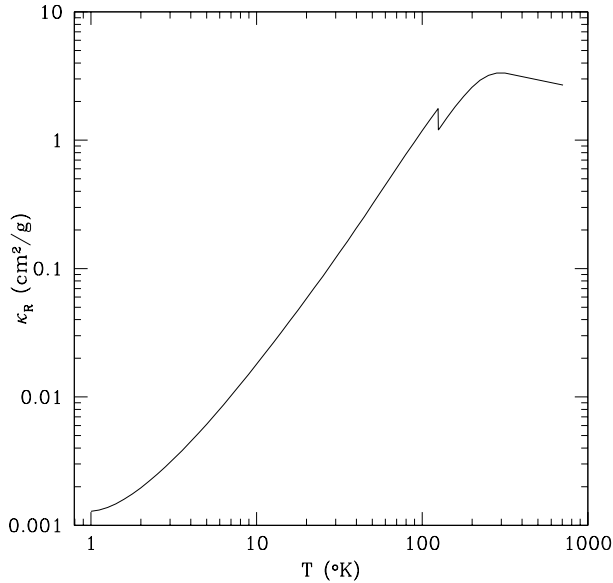


Fig. 3.— The Rosseland mean opacity for  $1\text{K} < T < 708\text{K}$ . For  $T < 316\text{K}$ , we have used the model of Yorke (1979) with the recent values for the extinction factor of Preibisch et al. (1993). For  $316\text{K} < T < 708\text{K}$ , we have used simple interpolated values. The jump around  $T \simeq 125\text{K}$  is due to the sublimation of the ice mantles.

model of Alexander & Ferguson (1994) for  $\kappa_R$ , which considered the absorption of atomic lines (with more than 8 million lines) and molecular lines (with nearly 60 million lines). Grain absorption and scattering due to silicates, iron, carbon and SiC have also been considered in this model. Alexander & Ferguson (1994) tabulated the opacity using a parameter,  $R$ , defined by

$$R = \frac{\rho}{T_6^3}, \quad (29)$$

where  $T_6^3$  is  $T/10^6$ . Figure 4 shows  $\kappa_R$  in the ranges  $-7 \leq \log R \leq 1$  and  $708\text{K} < T < 12500\text{K}$ . There are two jumps at  $T \simeq 1200\text{K}$  and  $2000\text{K}$  due to the sublimation of silicates and amorphous carbon, respectively. Therefore, all dust components evaporate at  $T \simeq 2000\text{K}$ , and the absorption of molecular and atomic lines becomes dominant above that temperature. Each curve in the figure is labeled with the value of  $\log R$ . For the intermediate temperature

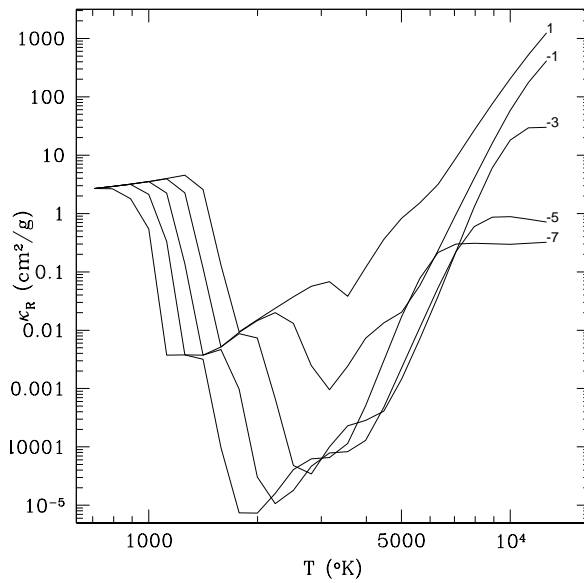


Fig. 4.— The Rosseland mean opacity as a function of temperature for  $708\text{K} < T < 12500\text{K}$  and  $-7 \leq \log R \leq 1$  (Alexander & Ferguson 1994). Each curve is labeled with the value of  $\log R$ . There are jumps at  $T \simeq 1200\text{K}$  and  $2000\text{K}$ . They are due to the sublimation of silicates and amorphous carbon, respectively. All dust components evaporate at  $T \simeq 2000\text{K}$ , and the absorption of molecular and atomic lines become the dominant coolant.

region ( $316\text{K} < T < 708\text{K}$ ), we have used simple interpolated values for  $\kappa_R$  (see Figure 3).

## 2.6. Thermodynamics

Temperature has been used as an independent variable in the iteration explained in section 2.4, and the specific internal energy of each particle is evaluated at every step of the iteration. The specific internal energy can be determined uniquely for a given temperature, density and chemical composition. For a more exact determination, the specific internal energies of hydrogen, helium and metals are calculated separately. We also consider the dissociation of hydrogen molecules in the energy calculation, but the ionization of hydrogen atoms is omitted, because ionization is negligible in the temperature range corresponding to our simulations. We now explain how to derive the energy. In this description,  $X$ ,  $Y$  and  $Z$  denote the mass fractions of hydrogen, helium and metals, respectively.

The total specific internal energy is given by

$$u = u(H) + u(H_2) + u(H_{2diss}) + u(He) + u(M). \quad (30)$$

Here  $u(H)$  is the specific internal energy of hydrogen atoms, given by

$$u(H) = \frac{3}{2} X y \frac{kT}{m_H}, \quad (31)$$

where  $k$  is the Boltzmann constant,  $m_H$  is the mass of the hydrogen atom, and  $y$  is the ratio of atomic to molecular hydrogen, given by

$$y = \frac{\rho(H)}{\rho X}, \quad (32)$$

where  $\rho(H)$  is the density of atomic hydrogen. In the equilibrium state,  $y$  is determined by

$$\frac{y^2}{1-y} = \frac{2.11}{\rho X} \exp \left[ \frac{52490}{T} \right] \quad (33)$$

(Aller 1963).

$u(H_2)$  is the specific internal energy of molecular hydrogen, given by

$$u(H_2) = \frac{X(1-y)E(H_2)}{2m_H}. \quad (34)$$

Here  $E(H_2)$  is the energy of hydrogen molecules, and is composed of three terms,

$$E(H_2) = \frac{3}{2}kT + E_{rot} + E_{vib}. \quad (35)$$

The terms of equation (35) are the translational, rotational and vibrational energies, respectively. The rotational energy of hydrogen molecules is composed of the contributions of *ortho*- and *para*-H<sub>2</sub>, and is given by

$$E_{rot} = k \frac{(1 - f_o)z_p T^2 \frac{\partial \ln z_p}{\partial T} + f_o z_o T^2 \frac{\partial \ln z_o}{\partial T}}{(1 - f_o)z_p + f_o z_o}, \quad (36)$$

where  $f_o$  is the fraction for *ortho*-H<sub>2</sub>, and is 3/4 in the equilibrium state. It is very hard to know the exact ratio between *ortho*- and *para*-H<sub>2</sub> in the star forming core, so we have used the equilibrium value in our simulations.  $z_o$  and  $z_p$  in equation (36) are the partition functions for *ortho*- and *para*-H<sub>2</sub>, respectively, and are given by

$$z_p = \sum_{j=0,2,4,\dots}^{\infty} (2j+1) \exp\left[\frac{-j(j+1)\theta_{rot}}{T}\right], \quad (37)$$

$$z_o = \sum_{j=1,3,5,\dots}^{\infty} (2j+1) \exp\left[\frac{-j(j+1)\theta_{rot}}{T}\right], \quad (38)$$

where  $\theta_{rot}$  is 85.4K. The vibrational energy for hydrogen molecules is given by

$$E_{vib} = \frac{k\theta_{vib}}{\exp(\theta_{vib}/T) - 1}, \quad (39)$$

where  $\theta_{vib}$  is 6100K.

The third term of equation (30) is the dissociation energy of hydrogen molecules, and is

$$u(H_{2diss}) = \frac{1}{2} \frac{XyD}{m_H}, \quad (40)$$

where  $D$  is the energy of dissociation for one molecule, and is 4.4773eV.

$u(He)$  and  $u(M)$  are the energies of helium and metals, respectively, and are given by

$$u(He) = \frac{3}{2} Y \frac{kT}{4m_H}, \quad (41)$$

$$u(M) = \frac{3}{2} Z \frac{kT}{A_m m_H}, \quad (42)$$

where  $A_m$  is the mean atomic number of metals, and is set to 16.78 in our simulation (Cameron 1968).

The specific internal energy of the gas is determined uniquely with equations (30) - (42) at a given temperature, and vice versa. However, an extra iteration is needed to derive the temperature from a given specific internal energy. Therefore, we have used  $T$  as an independent variable rather than  $u$  in our code.

### 3. Test for a nonisothermal collapse

#### 3.1. Initial conditions

MB93 developed an FDM code for radiation hydrodynamics, and performed simulations for a centrally condensed cloud. They used Cartesian and spherical codes, and the Eddington approximation for the treatment of radiative transfer. We have performed the same test of MB93 to compare our results. The comparison should be meaningful because the method of MB93 and ours are based on two completely different philosophies but deal with exactly the same problem.

The same initial conditions have been used in order to compare the results directly. The initial cloud has a mass of  $1.087M_{\odot}$  and a radius of  $1.1 \times 10^{16}$ cm. Solidbody rotation has been imposed around the  $z$ -axis, and the angular velocity is  $8.2 \times 10^{-12}\text{s}^{-1}$ .

The cloud is initially spherical but centrally condensed, and its density profile is given by

$$\rho = \frac{\rho_i}{\sqrt{x^2 + 4y^2 + 4z^2}}, \quad (43)$$

where  $\rho_i = 4.28 \times 10^{-16}\text{g/cm}^3$ . To implement this density profile, we have changed the mass of the particles according to their position. The mass of an individual particle is given by

$$m = \frac{m_i}{\sqrt{x^2 + 4y^2 + 4z^2}}, \quad (44)$$

where  $m_i = 1.087M_{\odot}/\mathcal{N}_{total}$ , and  $\mathcal{N}_{total}$  is the total number of particles used in the simulation. We have used 50000 particles. If the isothermal collapse stage lasts up to  $\rho \sim 10^{-13}\text{g/cm}^3$ , this is a sufficient number of particles<sup>3</sup> to satisfy the numerical Jeans condition (Truelove et al. 1997; Bate & Burkert 1997; Truelove et al. 1998; Whitworth 1998; Boss et al. 2000). MB93 chose this initial density profile to see the effect of radiative transfer and heating immediately, and to mimic the prolateness in star forming cores (Myers et al. 1991).

#### 3.2. Equation of state

The temperature of the cloud is set to 10K initially, and the thermal evolution during the collapse has been tracked using the implicit radiative transfer method explained in section 2.4. For comparison, we have performed three tests. The only difference between each test

---

<sup>3</sup>We assume that all particles have the same mass for checking the numerical Jeans condition.



is the calculation of the specific internal energy. Tests 1 and 2 use the energy equation of state of an ideal gas for the derivation of the energy, which is given by

$$u = \frac{1}{\gamma - 1} \frac{kT}{\mu m_h}, \quad (45)$$

where  $\mu$  is the mean molecular weight, and is given by

$$\mu = \left[ \frac{X(1-y)}{2} + \frac{Y}{4} + \frac{Z}{16.78} \right]^{-1}. \quad (46)$$

We have used  $\gamma = 5/3$  and  $7/5$  in Tests 1 and 2, respectively. The composition of the cloud is  $X = 0.70, Y = 0.27, Z = 0.03$  and  $y = 0$ , so  $\mu (= 2.385)$  is assumed to be constant. In Test 3, the more realistic energy calculation explained in section 2.6 has been used. Note that  $\mu$  is not constant in Test 3 due to the variation of  $y$ .

In all tests, the gas pressure,  $P$  is derived from the pressure equation of state,

$$P = \frac{\rho kT}{\mu m_H}. \quad (47)$$

### 3.3. Results

Figures 5 – 7 show the results of Tests 1, 2 and 3, respectively. They are snapshots at  $t \simeq 0.501t_{ff}^4$ . In the early stages of the collapse, the cloud contracts isothermally, and an elongated core forms in the center immediately due to the initial central condensation. The central core starts to trap the radiation and becomes adiabatic. The transition density from the isothermal to the adiabatic regimes is  $\sim 10^{-13}\text{g/cm}^3$ . This transition density is nearly the same in all simulations (See Figure 8). In the adiabatic stage, the temperature of the central core tends to increase quickly, while the outer parts of the collapsing cloud is still isothermal. The adiabatic core is easily distinguished in the temperature profile in Figures 5 – 7. The density is flatter in the core than in the outer parts of the cloud, and the infalling velocity drops suddenly at the edge of the core to form a shock wave. There is no big difference between the results of Tests 1, 2 and 3. However, the temperature of the central core in Test 1 is higher than that of Tests 2 and 3. The increase of the central temperature in Test 1 is faster than in the other simulations because of the higher  $\gamma$  value.

Figure 8 shows the evolution of the central core in the  $\rho - T$  plane. For comparison, we have drawn two straight lines which show the slopes for  $\gamma = 5/3$  and  $7/5$ . When the

---

<sup>4</sup>The freefall time ( $\simeq 3.38 \times 10^3\text{yrs}$ ) is evaluated with the assumption of a uniform density.

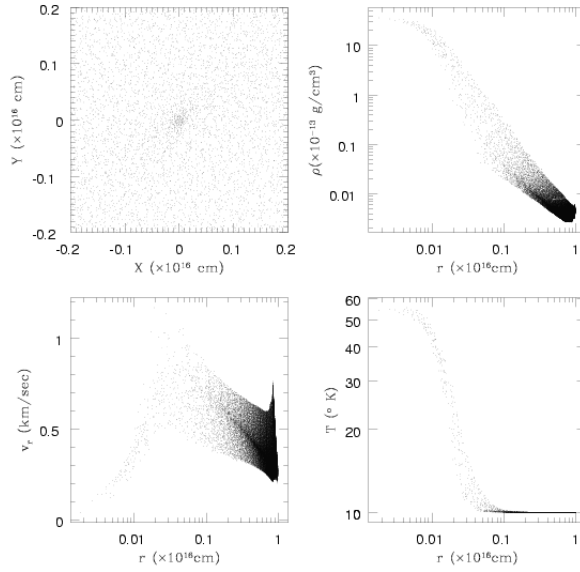


Fig. 5.— Results for TEST 1 ( $\gamma = 5/3$ ) at  $t = 0.5014t_{ff}$ . The top-left plate shows the particle positions near the center of the cloud. An elongated central core can be seen. The density profile (top right) of the core is nearly flat, and there is an accretion shock around the core in the velocity plot (bottom left). The outer envelope of the cloud remains isothermal ( $\simeq 10$ K) in the temperature plot (bottom right).

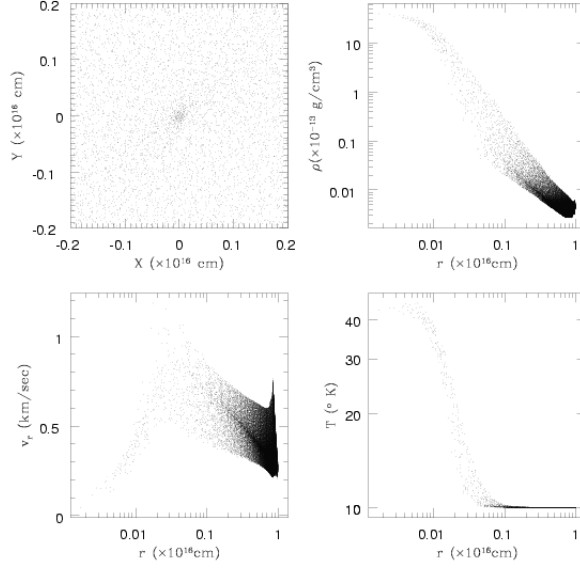


Fig. 6.— The results for TEST 2 ( $\gamma = 7/5$ ) at  $t = 0.5014t_{ff}$ . The overall features are very similar to those of Test 1, but the temperature of the central core is lower because of the smaller  $\gamma$  value.

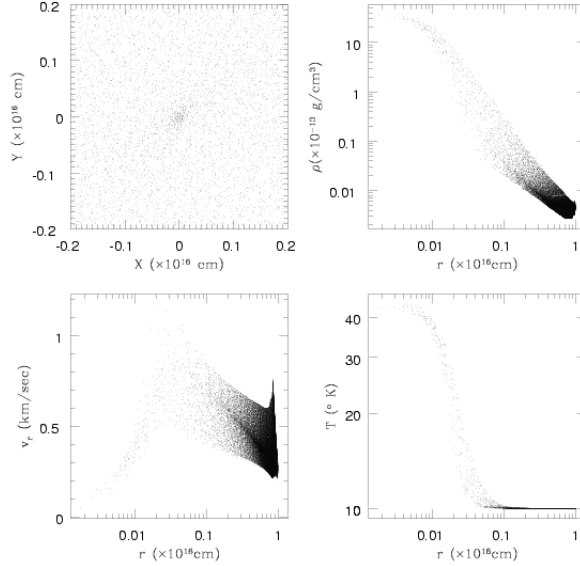


Fig. 7.— The results for TEST 3 (variable  $\gamma$ ) at  $t = 0.5016t_{ff}$ . They are more similar to those of Test 2.

central core enters the adiabatic regime, Tests 1 (dots) and 2 (long-dash) show slightly different evolutions. The slope of Test 1 is steeper than that of Test 2, so the temperature in Test 1 should be higher for the same density. In Test 3 (solid line), the evolution of central core follows  $\gamma = 5/3$  initially, but it becomes closer to  $\gamma = 7/5$  when the density becomes greater than  $\sim 10^{-12}\text{g/cm}^3$ . This change in slope is due to changes in the energy of hydrogen molecules. The rotational energy of hydrogen molecules is not important at very low temperatures, so the contribution of the translational energy is dominant. However, as the temperature increases, the rotational energy becomes more important, so the  $\gamma$  value gets closer to  $7/5$ . Could one use the  $\rho - T$  relation for the cloud center in Figure 8 and

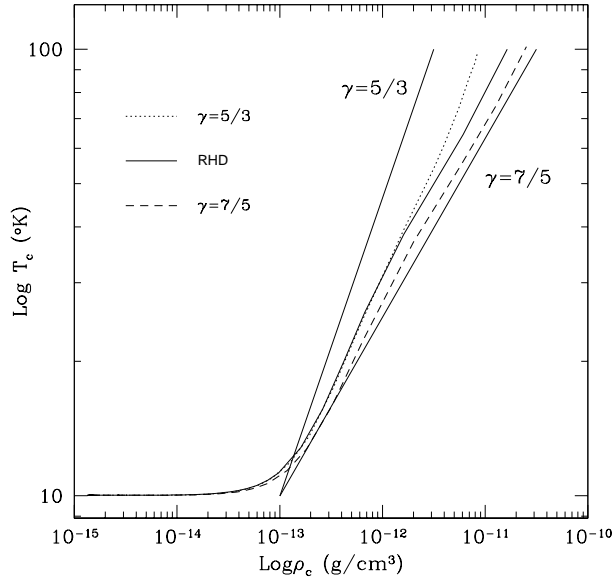


Fig. 8.— Evolution of the density and temperature of the cloud center. Dotted, long-dashed and solid lines are the results of Tests 1, 2 and 3, respectively. The temperature of the collapsing cloud is  $T \simeq 10\text{K}$  until  $\rho_c \simeq 10^{-13}\text{g/cm}^3$ , and then increases afterwards. The effective  $\gamma$  value for Test 3 is nearly  $5/3$  in  $10^{-13}\text{g/cm}^3 < \rho_c < 10^{-12}\text{g/cm}^3$ , and then changes to  $7/5$ , due to the excitation of the rotational energy of hydrogen molecules. All tests are stopped when the first core starts to expand.

apply it throughout the cloud, or even to other calculations? Figure 9 shows the  $\rho - T$  relation for all particles in Test 3 at  $t = 0.5309t_{ff}$ . The temperature of some particles in the density range of  $10^{-14}\text{g/cm}^3 \sim 10^{-13}\text{g/cm}^3$  is higher than the boundary value ( $= 10\text{K}$ ). Furthermore, there is a temperature dispersion at a given density through the cloud except at the lower densities. It is due to the non-spherically symmetric collapse, so particles closer to the central core are hotter. If a barotropic equation of state (Bodenheimer 1978; Cha &

Whitworth 2003a) were used in the simulation, all particles would lie on a line in the  $\rho - T$  plane without any dispersion, because there would be no thermal interaction between the hot central core and its surroundings.

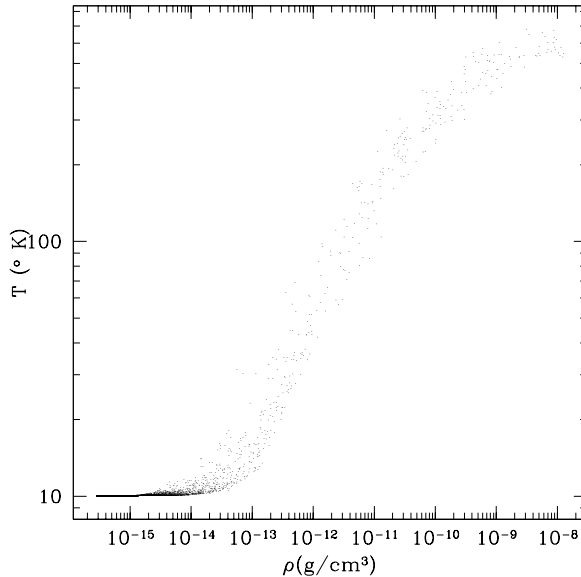


Fig. 9.— The  $\rho - T$  relation for all particles in Test 3 at  $t = 0.5309t_{ff}$ . The overall trend coincides well with that of Figure 8, but all particles are not on a line. The dispersion in the particle distribution is due to the thermal interaction between the hot central core and its surroundings, so some particles in the density range  $10^{-14}\text{g/cm}^3 \sim 10^{-13}\text{g/cm}^3$  show a higher temperature than the boundary value ( $= 10\text{K}$ ).

### 3.4. Comparison with MB93

We compare our results with those of MB93 in Table 2. CC and SC in the table mean Cartesian and Spherical codes, respectively. There are small differences in the results, the temperatures of SPH are lower than those of MB93. We may presume some reasons for this discrepancy. First of all, the treatment for radiative transfer is different. We have used the diffusion approximation in the simulations, while MB93 used the Eddington approximation. It is not easy to predict the resultant difference due to the different treatments for the radiative transfer, but the diffusion approximation may reduce the temperature increase (Larson 1969).

Secondly, there is a difference in the energy calculation of hydrogen molecules. We have

used equations (34) - (39), but MB93 used slightly different forms for  $u(H_2)$ . According to the  $u(H_2)$  calculation of Boss (1984) (See Appendix B of Boss (1984)), the transition temperature from  $\gamma = 5/3$  to  $7/5$  is 100K. However, in our calculation the transition temperature is variable, and  $\simeq 40$ K in Test 3. Therefore, the temperature increase should be slower in our simulation.

#### 4. Summary

We have presented a fully three-dimensional radiation hydrodynamic code based on the SPH method and the diffusion approximation. The difficulty encountered in previous attempts of how to treat the double derivative in SPH was solved by using the treatment developed by B85 to convert the double derivative to a single one. A thermal conduction test shows that this treatment works as expected.

The second difficulty arises from the large difference between the radiative and dynamical time scales. The radiative time scale is much shorter than the dynamical time scale in a collapsing cloud, especially in the isothermal stage. We have developed a fully three-dimensional implicit scheme for dealing with the large difference between the time scales.

To test our implicit scheme, we performed a nonisothermal cloud collapse of a centrally condensed cloud. The same simulation has been performed by MB93 using two FDM codes, and we have compared our results with those of MB93. The two numerical methods based on two completely different philosophies agree with each other.

Table 2: The central density and temperature

case	$\rho_c = 2.2 \times 10^{-12} \text{g/cm}^3$	$\rho_c = 1.7 \times 10^{-12} \text{g/cm}^3$
Test 1	49.9K	42.6K
Test 2	39.2K	34.3K
Test 3	41.0K	36.8K
CC	67.0K	
SC		56.0K

Comparison of our results with those of MB93. Here CC and SC mean Cartesian and Spherical codes, respectively.

## Acknowledgments

We thank Harold Yorke for providing a table of the new extinction values for grains and for a useful discussion. This research was supported by a grant from the National Sciences and Engineering Research Council of Canada. SHC thanks the Carnegie Institution of Canada for supporting his post-doctoral fellowship at Université de Montréal.

## REFERENCES

- Alexander, D. R., & Ferguson, J. W. 1994, *ApJ*, 437, 879
- Aller, L. H. 1963, *The Atmospheres of the Sun and Stars* (Ronald Press, New York), 119
- Bate, M. R., & Burkert, A. 1997, *MNRAS*, 288, 1060
- Bell, K. R., & Lin, D. N. C. 1994, *ApJ*, 427, 987
- Benz, W. 1990, in *The Numerical Modeling of Nonlinear Stellar Pulsations*, ed. J. R. Buchler (Kluwer Academic Publishers, Dordrecht), 269–288
- Bodenheimer, P. 1978, *ApJ*, 224, 488
- Boss, A. P. 1984, *ApJ*, 277, 768
- Boss, A. P., Fisher, R. T., Klein, R. I., & McKee, C. F. 2000, *ApJ*, 528, 325
- Brookshaw, L. 1985, *Publ. Astron. Soc. Aust.*, 6, 207 (B85)
- Cameron, A. G. W. 1968, in *Origin and Distribution of the elements*, ed. L. H. Ahrens (Pergamon Press, Toronto)
- Cha, S.-H., & Whitworth, A. P. 2003a, *MNRAS*, 340, 91
- . 2003b, *MNRAS*, 340, 73
- Cleary, P. W., & Monaghan, J. J. 1999, *J. Comp. Phys.*, 148, 227 (CM99)
- Gingold, R., & Monaghan, J. J. 1977, *MNRAS*, 181, 375
- Hernquist, L., & Katz, N. 1989, *ApJ*, 70, 419
- Larson, R. B. 1969, *MNRAS*, 145, 271
- Lodato, G., & Clarke, C. J. 2004, *ApJ*, 353, 841

- Low, C., & Lynden-Bell, D. 1976, MNRAS, 176, 367
- Lucy, L. B. 1977, AJ, 82, 1013
- Masunaga, H., & Inutsuka, S. I. 2000, ApJ, 531, 350
- Masunaga, H., Miyama, S. M., & Inutsuka, S. I. 1998, ApJ, 495, 346
- Monaghan, J. J. 1989, J. Comp. Phys., 82, 1
- . 1992, A&AR, 30, 543
- . 1997, J. Comp. Phys., 136, 298
- Monaghan, J. J., & Lattanzio, J. C. 1984, Publ. Astron. Soc. Aust., 5, 493
- Morris, J. P., & Monaghan, J. J. 1997, J. Comp. Phys., 136, 41
- Myers, P. C., Fuller, G. A., Goodman, A. A., & Benson, P. J. 1991, ApJ, 376, 561
- Myhill, E. A., & Boss, A. P. 1993, ApJS, 89, 345 (MB93)
- Oxley, S., & Woolfson, M. M. 2003, MNRAS, 343, 900
- Preibisch, T., Osenkopf, V., Yorke, H. W., & Henning, T. 1993, A&A., 279, 577
- Press, W. H., Teukolsky, S. A., Vetterling, W. T., & Flannery, B. P. 1992, Numerical Recipes, 2nd edn. (Cambridge University Press, New York)
- Rees, M. J. 1976, MNRAS, 176, 483
- Silk, J. 1977, ApJ, 214, 152
- Smith, R. C. 1977, MNRAS, 179, 521
- Truelove, J. K., Klein, R. I., McKee, C. F., Holliman, J. H., Howell, L. H., & Greenough, J. A. 1997, ApJ, 489, L179
- Truelove, J. K., Klein, R. I., McKee, C. F., Holliman, J. H., Howell, L. H., Greenough, J. A., & Woods, D. T. 1998, ApJ, 495, 821
- Viau, S. 2001, PhD thesis, Université de Montréal
- Whitehouse, S. C., & Bate, M. R. 2004, MNRAS, 353, 1078
- Whitworth, A. P. 1998, MNRAS, 296, 442



Winkler, K.-H. A., & Newman, M. J. 1980a, ApJ, 236, 201

—. 1980b, ApJ, 238, 311

Yorke, H. W. 1979, A&A., 80, 308

—. 1980, ApJ, 85, 215